ELSEVIER

Contents lists available at ScienceDirect

Chemical Engineering Journal

journal homepage: www.elsevier.com/locate/cej





Rapid electron transfer via imine-linked interface in dinuclear cobalt MOF@COF Z-scheme heterojunction for enhanced photocatalytic CO₂ reduction with H₂O

Yu-Chen Wang, Wen-Jie Shi^{*}, Ji-Hong Zhang, Wei-Xue Tao, Di-Chang Zhong^{*}, Tong-Bu Lu

Institute for New Energy Materials and Low Carbon Technologies, School of Materials Science and Engineering, Tianjin University of Technology, Tianjin 300384, China

ARTICLE INFO

Keywords: Covalent organic frameworks Metal organic frameworks Hybrid materials Imine-linked interface Photocatalytic CO_2 reduction

ABSTRACT

Crystalline and porous covalent organic frameworks (COFs) and metal organic frameworks (MOFs) materials have garnered significant interest in the field of photocatalytic CO_2 reduction due to their tunable band gaps. Despite extensive research on MOF-COF hybrid materials as semiconductor photocatalysts has been dedicated, exploration of intrinsic mechanisms and in-depth understanding of imine linker between the surface of MOF and COF are still limited. Herein, we designed a dinuclear hybrid photocatalyst, where TTA-TTB COF is in-situ grown on Co_2 -MOF-NH2 via imine bonding, forming a Z-scheme heterojunction. The introduction of this imine bonding between the Co_2 -MOF-NH2 core and TTA-TTB COF shell plays a crucial role in optimizing electron transfer kinetics. The imine bond facilitates the directional migration of photogenerated electrons from TTA-TTB COF to the Co_2 -MOF-NH2, promoting efficient charge separation and enhancing the photocatalytic activity. The resulting Co_2 -MOF-NH2-10@COF catalyst achieves a remarkable CO yield of 70.33 µmol g^{-1} h^{-1} for CO_2 -to-CO conversion under irradiation without additional sacrificial reductants. This yield is over 2.61 times higher than that of Co_2 -MOF-10@COF, which lacks the imine bonding interface, and 6.37 times higher than that of the TTA-TTB COF and Co_2 -MOF-NH2 mixture. This work offers new insights into the regulation of photogenerated carrier dynamics at the heterointerface and provides valuable guidance for the design of highly efficient Z-scheme photocatalysts for sustainable energy conversion.

1. Introduction

Photocatalytic reduction of CO_2 into value-added chemicals, particularly carbon monoxide (CO) with H_2O as electron donor has gained significant attention as a promising strategy for mitigating climate change and addressing global energy challenges [1–6]. However, the efficiency of photocatalytic CO_2 reduction is limited by several factors, including high activation barriers of CO_2 , slow electron transfer and poor charge separation, all of which will reduce the overall selectivity and efficiency of the photocatalytic system [7–12]. To overcome these issues, it is essential to design high-performance photocatalytic systems that not only enhance the activation of CO_2 but also optimize charge transfer processes.

Metal organic frameworks (MOFs) and covalent organic frameworks (COFs) are emerging as promising photocatalytic materials due to their high surface areas, tunable structures, and good stability under photocatalytic conditions (Scheme 1a) [13–19]. In recent years, hybrid

materials of MOF-COF photocatalytic have attracted much attention [20–23]. Theoretically, MOF-COF composites may be engineered to possess the superior catalytic capabilities of unsaturated MOF coordination metal centers together with the light absorption capacity by COF. The MOF and COF could be combined via several approaches, such as physical mixture and electrostatic interaction (Scheme 1b). Nevertheless, the MOF-COF composites still suffer from poor electron transfer kinetics and limited catalytic performance challenges in photocatalysis. Therefore, covalent-linking synthetic strategy is investigated to boost the charge transfer rate of MOF-COF composites [24–26]. However, the mechanisms of electron transfer at the engineered linking surface have not been thoroughly explored. Therefore, it is crucial to gain a deeper understanding of the role of surface linkers at the heterointerface of MOF-COF composites.

With the above considerations in mind, a dinuclear MOF@COF Z-scheme heterojunction (Co₂-MOF-NH₂-10@COF) was successfully fabricated, in which TTA-TTB COF is in-situ grown on Co₂-MOF-NH₂ via

E-mail addresses: wjshi@email.tjut.edu.cn (W.-J. Shi), dczhong@email.tjut.edu.cn (D.-C. Zhong).

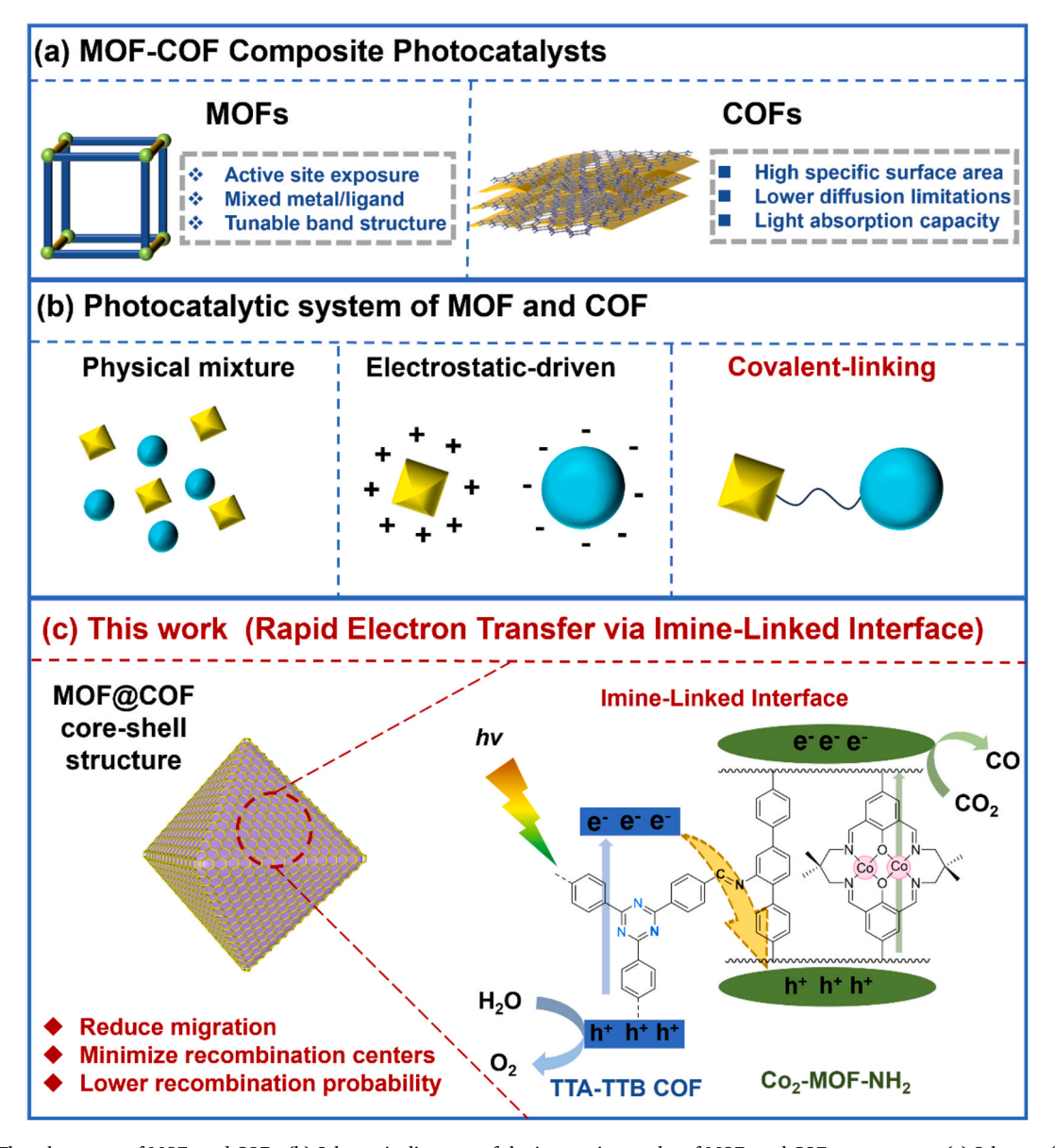
^{*} Corresponding authors.

imine bonding (Scheme 1c). The imine linkers changed the way in which the heterointerface is electronically structured and coordinated. Specifically, the introduction of imine bonds enhances the π -conjugation between the MOF and COF components, facilitating efficient charge transfer and promoting effective separation of photogenerated electronhole pairs. This structural modification results in a more favorable electronic alignment that supports the distinct roles of MOF in CO₂ reduction and COF in H₂O oxidation, thereby improving the overall photocatalytic performance of the MOF@COF system. The resulting Co₂-MOF-NH₂-10@COF catalyst demonstrates a remarkable CO yield of 70.33 μ mol g⁻¹ h⁻¹ under visible light when the H₂O as electron donor, which is over 2.61 times higher than the Co2-MOF-10@COF catalyst without imine bonding, and even 6.37 times higher than that of the MOF and COF mixture (TTA-TTB COF&Co₂-MOF-NH₂). electrochemical experiments revealed that the enhanced charge separation efficiency plays a crucial role in improving the photocatalytic performance of Co₂-MOF-NH₂-10@COF. These finding underscores the importance of molecularly engineered interfaces, specifically imine linkers, in optimizing photocatalytic systems for CO₂ reduction. By enhancing charge transfer and improving active site efficiency, this approach paves the way for the development of sustainable, high-performance photocatalysts, contributing to the realization of scalable solar-driven $\rm CO_2$ reduction technologies.

2. Experimental methods

2.1. Synthesis of TTA-TTB COF

TTA-TTB COF was synthesized following a modified literature procedure [27]. Typically, A 1,4-dioxane/mesitylene/3M HAc (v/v/v=10/10/1; 2.1 mL) mixture of 4,4′,4″-(1,3,5-triazine-2,4,6-triyl)trianiline (TTA, 8.86 mg, 0.025 mmol) and 4,4′,4″-(1,3,5-triazine-2,4,6-triyl)tribenzaldehyde (TTB, 9.85 mg, 0.025 mmol) was placed in a Pyrex tube (10 mL). After degassing by freeze–pump–thaw, the tube was sealed, and the reaction was conducted at 120 °C for 3 days. The yellow precipitate was collected by suction filtration, washed repeatedly with THF and then with acetone, and subjected to Soxhlet extraction with THF for 1 day. The powder was dried overnight under vacuum at 80 °C to afford the TTA-TTB COF in 80 % yield.



Scheme 1. (a) The advantages of MOFs and COFs. (b) Schematic diagrams of the integrating modes of MOFs and COFs components. (c) Scheme of charge transfer channel in artificial dinuclear MOF@COF Z-Scheme photosystem.

2.2. Synthesis of Co₂-MOF-NH₂ and Co₂-MOF

Co₂-MOF-NH₂ was synthesized according to the literature [28]. 5.2 mg ZrCl₄ (0.0222 mmol), 6.6 mg {Co₂(CH₃)₂C[CH₂N=CH(1-COOH-4-OH-3,5-C₆H₃)CH=NCH₂]₂C(CH₃)₂}(ClO₄)₂ (L1, 0.0074 mmol), 12.3 mg 2'-amino-[1,1'.4',1'' terphenyl]-4,4''-dicarboxylic acid (L2, 0.0370 mmol), 600 μ L acetic acid were dissolved in 6 mL DMF by ultrasound. Then the mixture was transferred into a 15 mL vial, which was sealed and heated at 120 °C for 24 h. After cooling to room temperature, the light-yellow powder was collected by centrifugation, washed with DMF and acetonitrile for 3 times.

Co₂-MOF was synthesized with slight modifications to the method used for Co₂-MOF-NH₂. 5.2 mg ZrCl₄ (0.0222 mmol), 6.6 mg {Co₂(CH₃)₂C[CH₂N=CH(1-COOH-4-OH-3,5-C₆H₃)CH=NCH₂]₂C (CH₃)₂}(ClO₄)₂ (L1, 0.0074 mmol), 11.8 mg [1,1':4',1''-terphenyl]-4,4''-dicarboxylic acid (L3, 0.0370 mmol), 600 μ L acetic acid and 200 μ L H₂O were dissolved in 6 mL DMF by ultrasound. Then the mixture was transferred into a 15 mL vial, which was sealed and heated at 120 °C for 24 h. After cooling to room temperature, the light-yellow powder was collected by centrifugation, washed with DMF, acetonitrile, dimethyl sulfoxide for 3 times.

2.3. Synthesis of Co_2 -MOF-N H_2 -x@COF (x=3, 5, 10, 20) and Co_2 -MOF-10@COF

Co₂-MOF-NH₂-x@COF (x = 3, 5, 10, 20) hybrid composites were fabricated by an in situ solvothermal reaction. Taking Co₂-MOF-NH₂-10@COF as example, the "Co₂-MOF-NH₂-10@COF" is specifically used to describe the photocatalyst in which 10 mg of amine-functionalized dinuclear cobalt-based MOF (Co₂-MOF-NH₂) is used as the core precursor for the in-situ growth of COF shell. Specifically, varying amounts of Co₂-MOF-NH₂ (3 mg, 5 mg, 10 mg, 20 mg), along with TTA (8.86 mg, 0.025 mmol) and TTB (9.85 mg, 0.025 mmol) were dispersed in a 1,4-dioxane/mesitylene/3M HAc mixture ($\nu/\nu/\nu = 10/10/1$; 2.1 mL) in a 10 mL Pyrex tube. After degassing by freeze–pump–thaw, the tube was sealed and heated at 120 °C for 3 days. The resulting yellow precipitate was collected by suction filtration, washed multiple times with THF and acetonitrile, and dried overnight under vacuum at 80 °C to yield the Co₂-MOF-NH₂-x@COF (x = 3, 5, 10, 20).

The synthesis of Co₂-MOF-10@COF followed the same procedure, substituting Co₂-MOF for Co₂-MOF-NH₂. Similarly, Co₂-MOF-NH₂-20@COF (L1:L2 = 1:1) was prepared using the same method as Co₂-MOF-NH₂-20@COF, but with Co₂-MOF-NH₂ (L1:L2 = 1:1) replacing Co₂-MOF-NH₂.

2.4. Photocatalytic experiment

The photocatalytic CO_2 reduction measurements were carried out in a gas–solid system. Initially, 1.0 mg photocatalysts was dispersed into 500 μ L acetonitrile through ultrasonication. Subsequently, the catalyst dispersion was deposited onto the surface of filter paper. Then, the filter paper and 100 μ L deionized water was loaded into the reactor, which was degassed with CO_2 for 20 min before irradiation. A 300 W Xe lamp was employed as light source ($\lambda=320\text{-}800\text{ nm}$), with the light intensity adjusted to 100 mW cm $^{-2}$. The generated gaseous products were analyzed with gas chromatography.

3. Results and discussion

3.1. Fabrication and characterization

The TTA-TTB COF was prepared by a thermo-polymerization reaction and the powder X-ray diffraction (PXRD) result confirmed the successful synthesis of TTA-TTB COF (Fig. S1). The crystalline nature of the synthesized dinuclear MOFs was first confirmed by PXRD. The PXRD patterns of Co₂-MOF-NH₂ and Co₂-MOF were found to match well with

the simulated pattern of UiO-68, indicating that the framework stability of the dinuclear MOFs was maintained after incorporating the Co2 metal sites (Fig. S2) [29]. This stability is crucial for ensuring the effectiveness of the catalysts during CO2 reduction reactions. Next, Co2-MOF-NH2x@COF (x = 3, 5, 10, 20) and Co_2 -MOF-10@COF samples were synthesized through a simple in-situ solvothermal method, as shown in Fig. 1a. PXRD patterns of these samples (Fig. 1b and Fig. S3) revealed that the characteristic peaks of both Co₂-MOF-NH₂ and TTA-TTB COF were clearly observed, confirming the successful integration of TTA-TTB COF onto the dinuclear MOFs. To further confirm the presence of both dinuclear MOFs and TTA-TTB COF, Fourier-transform infrared (FTIR) spectroscopy was performed. As shown in Fig. S4 and S5, the FTIR spectra of Co_2 -MOF-NH₂-x@COF (x = 3, 5, 10, 20) and Co_2 -MOF-10@COF exhibit the characteristic C=N stretching vibrations at 1608 cm⁻¹ and triazine rings at 1361 and 1506 cm⁻¹. These observations confirm the successful attachment of TTA-TTB COF onto the dinuclear

To confirm the presence of imine bonding between the Co₂-MOF-NH₂ and TTA-TTB COF, X-ray photoelectron spectroscopy (XPS) was employed (Fig. S6-S8). Due to the low content of Co(II) in Co₂-MOF-NH₂-10@COF, a dinuclear Co₂-MOF-NH₂ (L1:L2 = 1:1) sample with higher Co(II) concentration was synthesized. This was subsequently used to construct the Co₂-MOF-NH₂-20@COF (L1:L2 = 1:1) composite photocatalyst, enabling the detection of the Co(II) signal via XPS. The successful synthesis of Co₂-MOF-NH₂-20@COF (L1:L2 = 1:1) was initially confirmed by the PXRD patterns shown in Fig. S9. The XPS Co 2p peaks at 781.31 eV and 796.80 eV correspond to the Co 2p_{3/2} and Co 2p_{1/2} binding energies, respectively, revealing that the Co(II) oxidation state is preserved in the hybrid catalyst (Fig. S10 and S11) [30]. Additionally, Zr 3d_{5/2} and Zr 3d_{3/2} peaks at 184.88 eV and 182.52 eV confirmed the tetravalent state of Zr in the MOF structure (Fig. S12), Zr $3d_{5/2}$ and Zr $3d_{3/2}$ peaks at 185.13 eV and 182.78 eV confirmed the tetravalent state of Zr in the hybrid catalyst (Fig. S13) [31]. In the C1 s region, the peak can be deconvoluted into three distinct components: C=N (286.45 eV), C-C (284.97 eV), and C=O (289.27 eV). Notably, a decrease in the intensity of the C=O bond after the TTA-TTB COF coating, compared to Co₂-MOF-NH₂-20@COF (L1:L2 = 1:1), further supports the successful incorporation of COF into the MOF framework (Fig. S14) [32]. In the N 1 s spectrum, the disappearance of the -NH₂ peak at 399.52 eV and the emergence of a new peak corresponding to the C=N bond at 398.43 eV in Co₂-MOF-NH₂-20@COF (L1:L2 = 1:1) provide strong evidence for the formation of the covalent imine linkage during the in-situ growth of TTA-TTB COF onto the dinuclear Co₂-MOF-NH₂ framework (Fig. 1c). These XPS results conclusively demonstrate the successful formation of the imine bond between Co2-MOF-NH2 and TTA-TTB COF.

The scanning electron microscopy (SEM) image of Co₂-MOF-NH₂ reveals a well-defined octahedral morphology, while the TTA-TTB COF exhibits a granular morphology (Fig. S15 and S16). After the in-situ growth of TTA-TTB COF on Co2-MOF-NH2, the Co2-MOF-NH2-10@COF composite shows a distinct core-shell structure (Fig. S17). Transmission electron microscopy (TEM) and aberration-corrected TEM (AC-TEM) images further confirm the core-shell architecture, where the Co2-MOF-NH2 core is effectively encapsulated by the TTA-TTB COF shell (Fig. 1d and Fig. S18). Moreover, High-angle annular dark-field scanning transmission electron microscopy (HAADF-STEM) and energy dispersive spectroscopy (EDS) mapping reveals a well-defined interface between Co₂-MOF-NH₂ and TTA-TTB COF with clear spatial distributions of C, N, O, Co, and Zr elements (Fig. 1e and Fig. S19). The Co content in Co₂-MOF-NH₂-10@COF was confirmed to be 1.15 % by inductively coupled plasma mass spectrometry (ICP-MS). These results confirm the successful encapsulation of Co2-MOF-NH2 within the TTA-TTB COF shell. The core-shell morphology preserves the porosity of materials, creating efficient pathways for mass transfer and enhancing CO2 enrichment. The porosity of Co2-MOF-NH2, TTA-TTB COF, and Co2-MOF-NH2-10@COF was determined by the N2 sorption isotherms

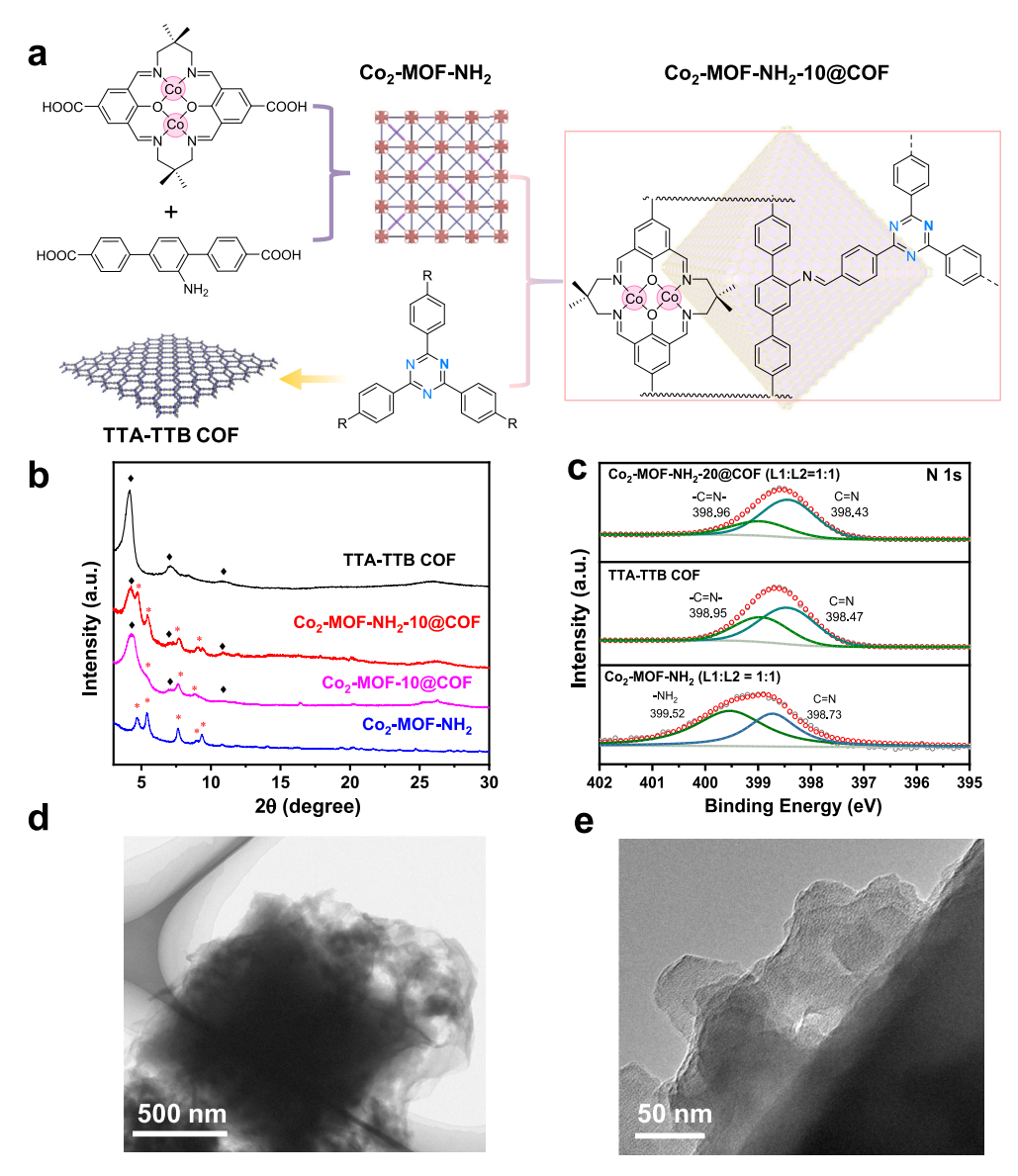


Fig. 1. (a) The schematic synthesis of Co_2 -MOF-NH₂-10@COF, the R in the scheme presented the CHO or NH₂ functional group. (b) The PXRD patterns of TTA-TTB COF, Co_2 -MOF-NH₂-10@COF, Co_2 -MOF-NH₂-10@COF, Co_2 -MOF-NH₂-10@COF, Co_2 -MOF-NH₂-10@COF. (e) HRTEM image of Co_2 -MOF-NH₂-10@COF.

measured at 77 K. As shown in Fig. S20, the S_{BET} of the Co_2 -MOF-NH₂ was 85.57 m² g⁻¹, which increased significantly to 190.28 m² g⁻¹ upon incorporation of TTA-TTB COF. The corresponding pore size distribution curves indicate that the hybrid material retains a predominant microporous structure, derived from both MOF and COF components. Co_2 -MOF-NH₂, TTA-TTB COF, and Co_2 -MOF-NH₂-10@COF all exhibit CO_2 adsorption capacities as demonstrated in Fig. S21. Finally, Thermogravimetric Analysis (TGA) was conducted to evaluate the thermal stability of the photocatalysts. The TGA curves (Fig. S22) show that both photocatalysts maintain excellent stability, which is critical for their long-term photocatalytic performance.

3.2. Energy band structures and interfacial interaction

To obtain the redox thermodynamic data of $\mathrm{Co_2\text{-}MOF\text{-}NH_2}$ and TTA-TTB COF, the energy band structures of the Z-scheme heterojunction were examined by UV–visible diffuse reflectance spectroscopy (UV-Vis DRS), Motty Schottky curves and ultraviolet photoelectron spectroscopy (UPS) measurements. As shown in Fig. S23, $\mathrm{Co_2\text{-}MOF\text{-}NH_2}$ and TTA-TTB COF exhibit adsorption edges at around 371 nm and 420 nm,

respectively. The UVvis DRS of Co₂-MOF-NH₂-x@COF (x = 3, 5, 20) samples were also depicted in Fig. S24. The band-gap energy (Eg) of Co₂-MOF-NH₂ and TTA-TTB COF were estimated as 1.89 eV and 2.40 eV by using the Kubelka-Munk (KM) method based on its solid UV-vis absorption spectroscopy (Fig. S25 and S26) [33-36]. Both materials are identified as n-type semiconductors, as evidenced by the positive slope of their Mott-Schottky curve. The flat band position (V_{fb}) of Co₂-MOF- NH_2 and TTA-TTB COF were determined as -1.14 and -0.99 V vs. NHE, respectively (Fig. S27 and S28). Considering that the conduction band (CB) typically lies approximately 0.10 V negative than the flat-band potential (V_{fb}) in n-type semiconductors [37]. The CB of Co₂-MOF-NH₂ and TTA-TTB COF were calculated to be -1.24 and -1.09 eV vs. NHE, respectively. Combing these CB values with the band gap results, the valence band (VB) of photocatalysts were estimated to be 0.65 eV vs. NHE for Co₂-MOF-NH₂ and 1.31 eV vs. NHE for TTA-TTB COF. Evidently, the CB potentials of both Co₂-MOF-NH₂ and TTA-TTB COF are more negative than the redox potential required for the photocatalytic reduction of CO_2 to CO (-0.52 V vs. NHE), thus satisfying the thermodynamic prerequisite for the conversion of CO₂ to CO [38–40]. Additionally, UPS measurements revealed the work function of Co2MOF-NH₂ and TTA-TTB COF were 5.32 eV and 5.57 eV vs. vacuum, respectively. And the Fermi energy levels (E_F) of Co_2 -MOF-NH₂ and TTA-TTB COF were -1.07 eV and -0.82 eV vs. NHE (Fig. S29 and S30), respectively. Based on these findings, the energy-band alignment of Co_2 -MOF-NH₂ and TTA-TTB COF was illustrated in Fig. 2a, confirming the successful formation of a Z-scheme heterojunction in Co_2 -MOF-NH₂-x@COF (x=3,5,10,20). This heterojunction is expected to enhance the charge separation efficiency during the photocatalytic reduction of Co_2 .

The formation of the Z-scheme heterojunction will facilitate the directed movement at the interfaces of composite materials. To further investigated the charge transfer process between the Co2-MOF-NH2 and TTA-TTB COF, in situ X-ray photoelectron spectroscopy (XPS) spectra and EPR measurements were carried out. As shown in Fig. 2b, the Co $2p_{1/2}$ and Co $2p_{3/2}$ binding energies in Co₂-MOF-NH₂-20@COF (L1:L2 = 1:1) exhibit a positive shift to 781.31 eV and 796.80 eV, respectively, compared to those in Co₂-MOF-NH₂. This positive shift indicates the establishment of a built-in electric field at the interface between dinuclear MOF and TTA-TTB COF. Under illumination, Zr 3d binding energies remain unchanged (Fig. S31), while Co 2p peaks shift negatively, indicating electron accumulation at Co sites within Co₂-MOF-NH₂. This confirms Co as the primary active center for CO2 reduction, and the imine bonds facilitate the rapid transfer of charge carriers, enhancing the charge separation efficiency. In contrast, for the composite without imine bonding, Co₂-MOF-20@COF (L1:L2 = 1:1), the XPS spectra show positive shifts in the Co $2p_{1/2}$ and Co $2p_{3/2}$ peaks to 796.83 eV and 781.06 eV, respectively, indicating the formation of an interfacial electric field. Upon illumination, the binding energies also shift negatively, but to a lesser extent, with Co $2p_{1/2}$ and Co $2p_{3/2}$ peaks shifting to 780.91 eV and 796.72 eV, respectively. The less pronounced shifts in comparison to Co₂-MOF-20@COF (L1:L2 = 1:1) suggest a weaker interfacial electric field and less efficient charge separation in Co2-MOF-20@COF (Fig. S32). This comparative analysis clearly demonstrates that the introduction of imine bonding strengthens the interfacial interaction between Co₂-MOF-NH₂ and TTA-TTB COF, leading to the formation of a more robust built-in electric field. This improved interaction significantly enhances charge carrier separation, which is essential for efficient photocatalytic performance.

To further investigate the role of imine bonding in charge transfer dynamics, EPR measurements were conducted using DMPO as a sensitive probe to detect the formation of hydroxyl radicals (·OH) and superoxide anions (·O₂) on the surfaces of Co₂-MOF-NH₂-10@COF, Co₂-MOF-10@COF and the control samples [41–43]. In the absence of light, no signals corresponding to DMPO--OH or DMPO-- O_2^- were observed for all these materials (Fig. S33 and S34). However, under light irradiation, the signal corresponding to DMPO- \cdot O₂ in the Co₂-MOF-NH₂-10@COF was significantly stronger than that observed in the Co₂-MOF-10@COF composites without imine bonding, and the control samples, suggesting that the imine bonding promotes more efficient photogenerated charge separation in the hybrid material (Fig. S35 and S36). Conversely, no distinct DMPO-OH signal was observed for all samples, likely due to their insufficient oxidizing potential to oxidize H₂O to ·OH (1.90 V vs. NHE) (Fig. S37) [44]. These findings strongly indicate that imine bonding enhances the built-in electric field in the Z-scheme heterojunction, playing a crucial role in improving the separation efficiency of photogenerated charge carriers during photocatalysis.

To gain deeper insights into the spatial distribution of electron-hole pairs in the MOF@COF system with an imine bond linker, time-dependent density functional theory (TD-DFT) calculations and electron-hole excitation analyses were conducted. By comparing the action spectra with the simulated energy spectra (Fig. S38), ES1 was identified as the primary excited state contributing to the overall reaction. In the population analysis (Fig. 2c), the photogenerated electrons and holes in ES1 are prominently highlighted. This state exhibits a higher distribution density of electrons and holes on the molecular fragment model of dinuclear MOF@COF with an imine bond linker. Molecular orbital analysis further revealed that the highest occupied molecular orbital (HOMO) and the lowest unoccupied molecular orbital (LUMO) are localized at different component (Fig. S39). This spatial

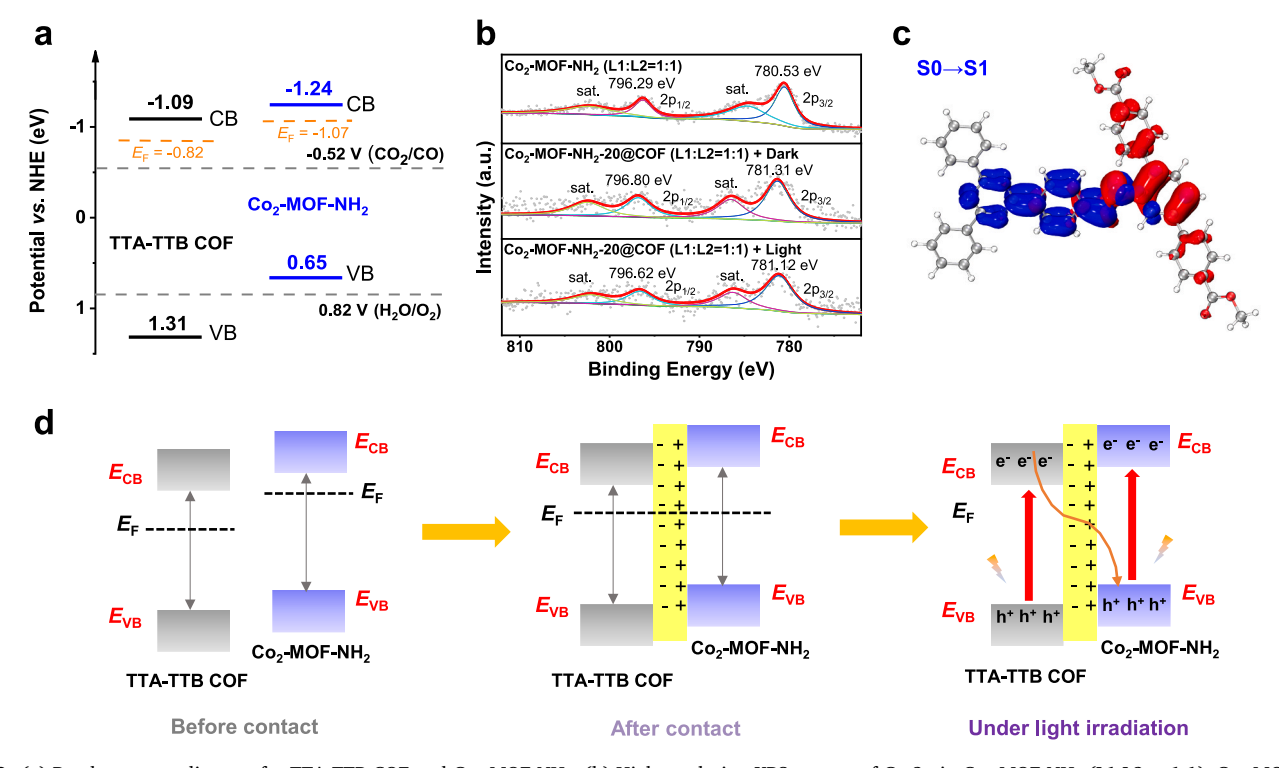


Fig. 2. (a) Band-structure diagram for TTA-TTB COF and Co_2 -MOF-NH₂. (b) High-resolution XPS spectra of Co_2 more Co_2 -MOF-NH₂ (L1:L2 = 1:1), Co_2 -MOF-NH₂-20@COF (L1:L2 = 1:1) before and after irradiation. (c) Electron and hole populations for the ES1 excited state of the molecular fragment model of dinuclear MOF@COF with imine bond linker. (d) Energy band structure and charge transfer in TTA-TTB COF and Co_2 -MOF-NH₂ before and after contact as well as charge transfer pathway in Co_2 -MOF-NH₂-x@COF under light irradiation.

separation of HOMO and LUMO indicates an effective charge separation facilitated by the enhanced π -conjugation between the MOF and COF through the imine bond linker. The electrostatic potential (ESP) map and projected density of states (PDOS) further reveal a built-in electric field across the interface of MOF@COF and confirm the electron-accepting nature of the Co centers at the reduction site, respectively (Fig. S40 and S41). These results suggest that the introduction of an imine bond linker promotes the separation of electrons and holes during photoexcitation, thereby enhancing the photocatalytic efficiency of the MOF@COF system.

Based on these observations, the proposed charge transfer pathway in Co₂-MOF-NH₂-x@COF is illustrated in Fig. 2d. The Fermi energy ($E_{\rm F}$) level of Co₂-MOF-NH₂ is more negative than that of the TTA-TTB COF, which facilitates free electron transfer from Co₂-MOF-NH₂ to the TTA-TTB COF, thereby establishing a built-in electric field at the interface. This interfacial electron transfer occurs due to the difference in $E_{\rm F}$ between Co₂-MOF-NH₂ and TTA-TTB COF, leading to the alignment of their energy levels. Under light irradiation, excited electrons rapidly migrate from the conduction band (CB) of TTA-TTB COF to the valence band (VB) of Co₂-MOF-NH₂, with the CB of Co₂-MOF-NH₂ then participating in CO₂ reduction. Simultaneously, the holes generated in the VB of TTA-TTB COF are involved in the oxidation of H₂O to O₂. This process highlights the critical role of the Z-scheme heterojunction and imine bonding in facilitating efficient charge transfer, thereby enhancing the overall photocatalytic performance.

3.3. Photocatalytic performance

Encouraged by the analysis above, the CO2 reduction reactions were

conducted along with Co_2 -MOF-NH₂-x@COF (x = 3, 5, 10, 20) hybrid materials as photocatalysts in the gas-solid photocatalytic system, 100 μL water was introduced into the catalytic reactor to generate vapors under irradiation (Fig. S42). The gaseous products were detected by gas chromatography after illumination for 10 h and there is no liquid products produced in the CO₂ reduction process (Fig. S43). As shown in Fig. 3a and Fig. S44-S45, the optimized photocatalysts Co₂-MOF-NH₂-10@COF presented best CO generation rates of 70.33 µmol g⁻¹h⁻¹ (Co₂-MOF-NH2-3@COF, Co2-MOF-NH2-5@COF, and Co2-MOF-NH2-20@COF are 18.16 µmol g⁻¹h⁻¹, 44.28 µmol g⁻¹h⁻¹, and 36.83µmol g⁻¹h⁻¹, respectively) with a CO selectively of over 99 % (Fig. S46). The yield is significantly 23.29, 12.63, 6.37, and 2.61 times higher compared to TTA-TTB COF, Co2-MOF-NH2, TTA-TTB COF&Co2-MOF-NH2, and Co2-MOF-10@COF, respectively. Moreover, this yield is comparable to that of some reported MOF-COF catalysts (Table S1). The O2 generated from the photocatalytic oxidation of H₂O was also collected, showing a CO/ O₂ ratio of approximately 2:1 (Fig. S47). The quantum yield of Co₂-MOF-NH₂-10@COF for photocatalytic CO₂ reduction was determined to be 0.046 % at 450 nm. It can be explained that the fast electron transfer channel at the heterointerface of Co2-MOF-NH2 and TTA-TTB COF builds a more efficient nonradiative decay pathway.

A series of control experiments on $\text{Co}_2\text{-MOF-NH}_2\text{-}10@\text{COF}$ were conducted to identify the key factors for CO_2 reduction. As shown in Fig. 3b, when the photocatalytic CO_2 reduction reaction was conducted in the absence of CO_2 , water vapours or light, the CO product was detected trace. It was initially established that the CO originated from CO_2 , and suggested that H_2O served as the electron donor in the photocatalytic CO_2 reduction reaction. To confirm this speculation, $^{13}\text{CO}_2$ isotope trace experiment was carried out. The mass spectrum (MS) of m/

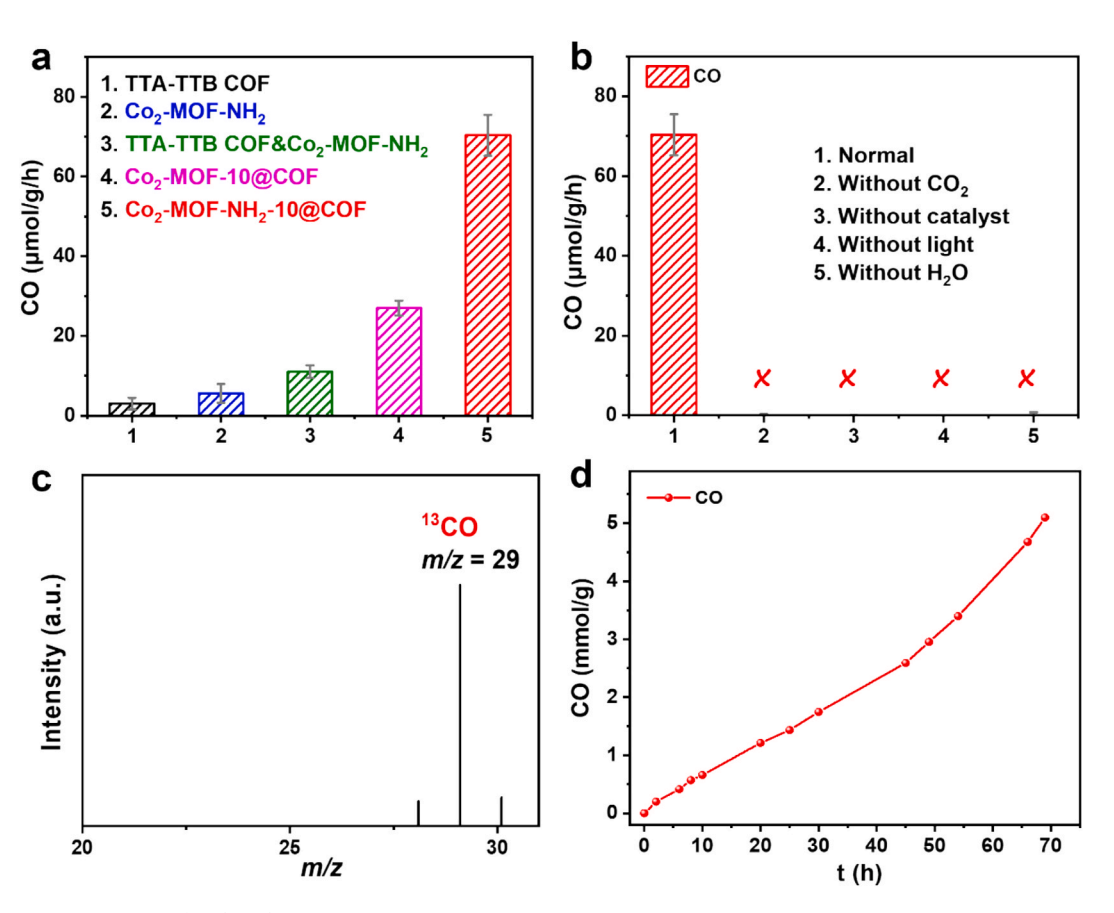


Fig. 3. (a) The CO generation rates of 10 h with TTA-TTB COF, Co_2 -MOF-NH₂, TTA-TTB COF& Co_2 -MOF-NH₂, Co_2 -MOF-NH₂, Co_2 -MOF-NH₂, Co_2 -MOF-NH₂-10@COF, Co_2 -MOF-NH₂-10@COF as the photocatalysts. (b) Control experiments of photocatalytic CO_2 reduction reaction for Co_2 -MOF-NH₂-10@COF. (c) Mass spectrum of the gaseous product generated in the photocatalytic $^{13}CO_2$ reduction over Co_2 -MOF-NH₂-10@COF. (d) The CO production during the long-term photocatalytic CO_2 reduction with Co_2 -MOF-NH₂-10@COF as the photocatalysts.

z=29 suggest that the CO originates from CO₂ (Fig. 3c) [45,46]. Moreover, the $\mathrm{H}_2^{18}\mathrm{O}$ isotope trace experiment was also conducted to identify the electron source for photocatalytic CO₂ reduction to CO. The MS of m/z=36 can be attributed to $^{18}\mathrm{O}_2$, indicating that the $\mathrm{H}_2\mathrm{O}$ serves as electron source for CO₂ photoreduction (Fig. S48) [47,48]. Besides activity, durability is also an important factor for evaluating the performance of catalysts. As displayed in Fig. 3d, Co₂-MOF-NH₂-10@COF exhibits no significant decrease in CO production rate after 60 h of irradiation, highlighting its excellent stability. This was further evidenced by PXRD, IR spectra and SEM image (Fig. S49-S51), which confirmed that the crystalline phase, composition and morphology of Co₂-MOF-NH₂-10@COF remain unchanged after photocatalysis, thus demonstrating its robust stability.

3.4. Mechanism study

Electrochemical impedance spectroscopy (EIS) and transient photocurrent response and were carried out to study charge transfer and separation efficiency of the photocatalysts. $\rm Co_2\text{-}MOF\text{-}NH_2\text{-}10@COF$ displays a smaller semicircular diameter of Nyquist curves compared with other photocatalysts (Fig. S52), indicating a smaller interfacial charge transfer resistance, verifying the efficient separation of photogenerated carriers. As shown in Fig. 4a, the photocurrent density of $\rm Co_2\text{-}MOF\text{-}NH_2\text{-}10@COF}$ is higher than that of other catalysts under light irradiation, indicating a faster charge transfer and lower carrier recombination rate. Photoluminescence (PL) spectra were collected to investigate the charge transfer and separation kinetics of the photocatalysts. Owing to the unique routes for charge transfer, the fluorescence intensity of $\rm Co_2\text{-}MOF\text{-}NH_2\text{-}10@COF}$ was the weakest compared with other catalysts as shown in Fig. 4b, which leads to decreased charge

carrier lifetimes for Co₂-MOF-NH₂-10@COF ($au_{ave} = 0.34$ ns) in contrast to Co₂-MOF-10@COF ($\tau_{ave} = 0.73$ ns) and TTA-TTB COF ($\tau_{ave} = 2.40$ ns) (Fig. 4c; Table S2). Moreover, Kelvin probe force microscopy measurements showed that the surface potential of Co_2 -MOF-NH₂-10@COF (ΔE = 169.25 mV) is higher than that of pristine TTA-TTB COF ($\Delta E = 18.31$ mV), Co₂-MOF-NH₂ ($\Delta E = 34.79$ mV) and Co₂-MOF-10@COF ($\Delta E =$ 46.99 mV). Accordingly, a greatly enhanced built-in electric field favors the separation of photogenerated carriers and transfer (Fig. S53) [49]. Further, the binding of Co2-MOF-NH2-10@COF and Co2-MOF-NH₂@COF with CO₂ was explored experimentally by CO₂ temperature programmed desorption (TPD). As shown in Fig. S54, the signal intensity of CO2 desorption in Co2-MOF-NH2-10@COF was higher than that in Co₂-MOF-NH₂@COF in Co₂-MOF-NH₂-10@COF. This indicates a stronger binding affinity towards CO2, which in turn correlates with enhanced photocatalytic performance. The above results can be explained that the fast electron transfer channel at the heterointerface of Co₂-MOF-NH₂ and TTA-TTB COF builds a more efficient nonradiative decay pathway, thereby accelerating charge separation and electron transfer, and improving the catalytic reaction kinetics of artificial photosynthesis.

To demonstrate the reaction path of $\rm CO_2$ reduction in catalytic process, in situ FTIR measurements were carried out to detect the intermediates during the reaction on the surface of $\rm Co_2$ -MOF-NH₂- $\rm 10@COF$. As shown in Fig. 4d, the peak at 1638 and 2078 cm $^{-1}$ was presented the characteristic asymmetric expansion vibration of *COOH and $\rm CO^*$ intermediate, which are key intermediates for CO generation in $\rm CO_2$ reduction reaction [50]. Based on these results, a proposal reaction pathway was proposed for the photocatalytic $\rm CO_2$ reduction over dinuclear $\rm Co_2$ -MOF-NH₂ coated with TTA-TTB COF. Under irradiation, $\rm Co_2$ -MOF-NH₂- $\rm 10@COF$ absorbs photons, generating electron-hole

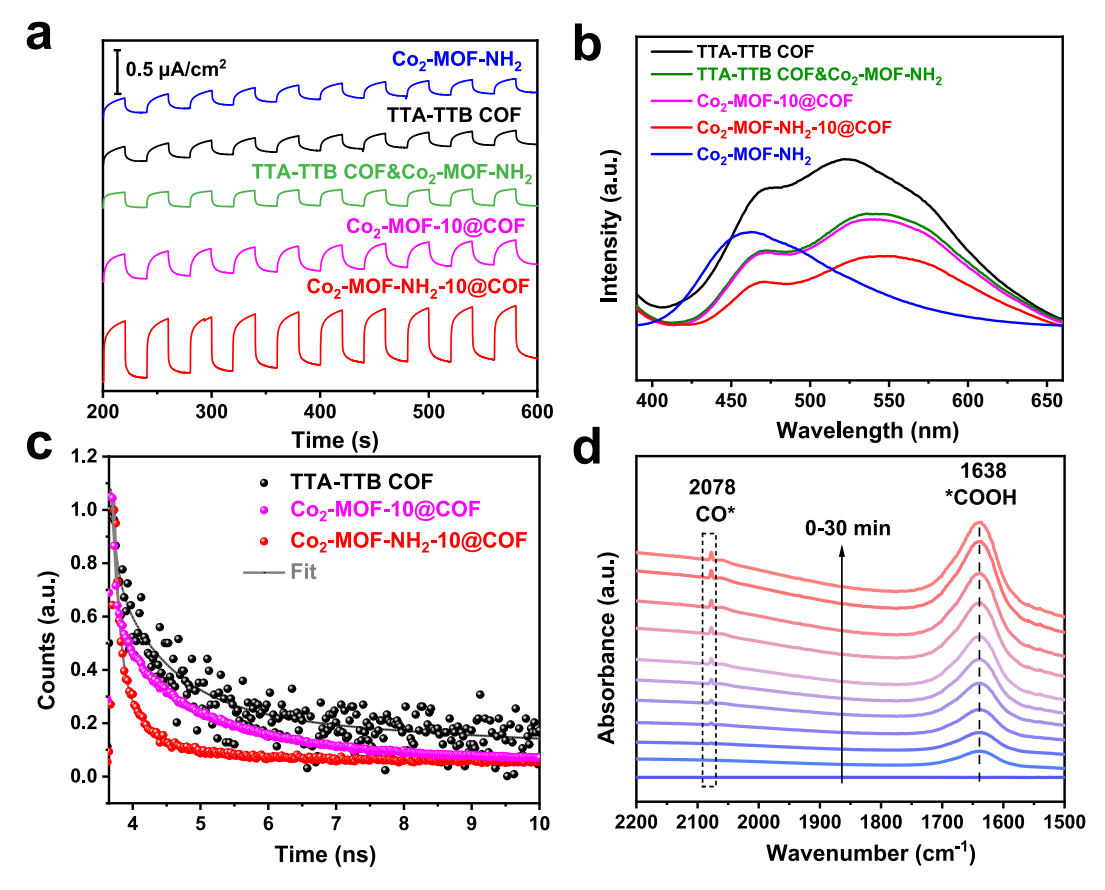


Fig. 4. (a) I-t curves and (b) PL spectra of TTA-TTB COF (black), TTA-TTB COF&Co₂-MOF-NH₂ (green), Co₂-MOF-10@COF (magenta), Co₂-MOF-NH₂-10@COF (red) and Co₂-MOF-NH₂ (blue). (c) Time-correlated PL decay traces of TTA-TTB COF, Co₂-MOF-10@COF, Co₂-MOF-NH₂-10@COF. (d) In situ FTIR spectra for photocatalytic CO₂ reduction over Co₂-MOF-NH₂-10@COF.

pairs. Subsequently, the photogenerated electrons were transferred through the imide bond, leading to the accumulation of photogenerated electrons and holes in Co₂-MOF-NH₂ and TTA-TTB COF, respectively. Then the photogenerated electrons in the Co₂-MOF-NH₂ catalyze CO₂ to CO through a *COOH pathway. As shown in Fig. S55, *COOH formation is endothermic (1.43 eV), while its conversion to *CO is exothermic (-0.73 eV), confirming the thermodynamic feasibility. Meanwhile, photogenerated holes in the valence band of TTA-TTB COF drive the oxidation of H₂O to producing O₂, thus realizing the artificial photocatalysis (Fig. S56).

4. Conclusions

In conclusion, a series of high-performance dinuclear complex-based MOF@COF catalysts for artificial photocatalytic CO2 reduction were elaborated by anchoring TTA-TTB COF on the surface of dinuclear Co₂-MOF-NH₂. Co₂-MOF-NH₂-10@COF shows significantly improved photocatalytic CO2 to CO reaction with H2O as sacrificial reactant in gas-solid system, with the CO yield of 70.33 μ mol g⁻¹ h⁻¹. This yield is approximately 12.63, 23.29, and 2.61 times higher than those of Co₂-MOF-NH₂, TTA-TTB COF and Co₂-MOF-10@COF, respectively. The results of experimental characterizations revealed that the microenvironment and local electronic structure of Z-scheme heterointerface were well engineered by imine bond. Meanwhile, imine bonds favor the formation of a close interface connection, as confirmed by DFT calculations demonstrating enhanced π -conjugation and efficient charge transfer between the MOF and COF components. As a result, this study may contribute to a better understanding of imine bonds and the development of alternative MOF@COF Z-scheme photocatalysts for advanced applications.

CRediT authorship contribution statement

Yu-Chen Wang: Writing – original draft, Methodology, Investigation. Wen-Jie Shi: Writing – review & editing, Supervision, Methodology. Ji-Hong Zhang: Investigation. Wei-Xue Tao: Investigation. Di-Chang Zhong: Writing – review & editing, Supervision, Methodology, Funding acquisition, Conceptualization. Tong-Bu Lu: Supervision.

Declaration of competing interest

The authors declare that they have no known competing financial interests or personal relationships that could have appeared to influence the work reported in this paper.

Acknowledgments

This work was supported by the National Key R&D Program of China (2022YFA1502902), the National Natural Science Foundation of China (22271218 and 22201209), and the Natural Science Foundation of Tianjin City (24JCZDJC00220).

Appendix A. Supplementary data

Supplementary data to this article can be found online at $\frac{\text{https:}}{\text{doi.}}$ org/10.1016/j.cej.2025.164327.

Data availability

Data will be made available on request.

References

- [1] S.-J. Davis, K. Caldeira, H.-D. Matthews, Future $\rm CO_2$ emissions and climate change from existing energy infrastructure, Science 329 (2010) 1330–1333.
- [2] Q. Wang, C. Pornrungroj, S. Linley, E. Reisner, Strategies to improve light utilization in solar fuel synthesis, Nat. Energy 7 (2022) 13–24.

- [3] M.-Q. Li, Z.-Q. Han, Q.-Y. Hu, W.-Y. Fan, Q. Hu, D.-P. He, Q.-X. Chen, X.-C. Jiao, Y. Xie, Recent progress in solar-driven CO₂ reduction to multicarbon products, Chem. Soc. Rev. 53 (2024) 9964.
- [4] X. Li, J. Yu, M. Jaroniec, X. Chen, Cocatalysts for selective photoreduction of CO₂ into solar fuels, Chem. Rev. 119 (2019) 3962–4179.
- [5] M. Malhotra, V. Soni, R. Kumar, P. Tarannuma, S. Singha, Q.-V. Thakur, L.-H. Le, V.-H. Nguyen, P.R. Nguyen, MOFs-based S-scheme heterojunction photocatalysts: challenges and prospects to break the selectivity limitation for intensified C1 products in CO₂ photoreduction, Chem. Eng. J. 506 (2025) 160238.
- [6] Y.-N. Gong, S. Wang, H.-J. Dong, J.-H. Mei, D.-C. Zhong, T.-B. Lu, Incorporating a binuclear cobalt polymer into mesoporous TiO₂ to construct a new Z-scheme heterojunction for boosting artificial photosynthesis, Appl. Catal. B 357 (2024) 124310.
- [7] S. Wang, B.-Y. Guan, Y. Lu, X.-W. Lou, Formation of hierarchical In₂S₃-CdIn₂S₄ heterostructured nanotubes for efficient and stable visible light CO₂ reduction, J. Am. Chem. Soc. 139 (2017) 17305–17308.
- [8] L. Zhang, R.-H. Li, X.-X. Li, J. Liu, W. Guan, L.-Z. Dong, S.-L. Li, Y.-Q. Lan, Molecular oxidation-reduction junctions for artificial photosynthetic overall reaction, Proc. Natl. Acad. U. S. A. 119 (2022) e2210550119.
- [9] J. Zhou, J. Li, L. Kan, L. Zhang, Q. Huang, Y. Yan, Y. Chen, J. Liu, S.-L. Li, Y.-Q. Lan, Linking oxidative and reductive clusters to prepare crystalline porous catalysts for photocatalytic CO₂ reduction with H₂O, Nat. Commun. 13 (2022) 4681.
- [10] Y.-Z. Cheng, W. Ji, P.-Y. Hao, X.-H. Qi, X. Wu, X.-M. Dou, X.-Y. Bian, D. Jiang, F.-T. Li, X.-F. Liu, D.-H. Yang, X. Ding, B.-H. Han, A fully conjugated covalent organic framework with oxidative and reductive sites for photocatalytic carbon dioxide reduction with water, Angew. Chem. Int. Ed. 62 (2023) e202308523.
- [11] H.-X. Li, R.-J. Li, G. Liu, M.-L. Zhai, J.-G. Yu, Noble-metal-free single- and dualatom catalysts for artificial photosynthesis, Adv. Mater. 36 (2024) 2301307.
- [12] Y.-X. Feng, K. Su, Z.-L. Liu, S.-X. Yuan, Y.-F. Mu, M. Zhang, T.-B. Lu, A halide perovskite based ternary heterojunction with multi-shell hollow structure for stable and efficient artificial photosynthesis, Appl. Catal. B 347 (2024) 123821.
- [13] H. Furukawa, K.E. Cordova, M. O'Keeffe, O.M. Yaghi, The chemistry and applications of metal-organic frameworks, Science 341 (2013) 1230444.
- [14] M. Lu, M. Zhang, J. Liu, Y. Chen, J.-P. Liao, M.-Y. Yang, Y.-P. Cai, S.-L. Li, Y.-Q. Lan, Covalent organic framework based functional materials: important catalysts for efficient CO₂ utilization, Angew. Chem. Int. Ed. 61 (2022) e202200003.
- [15] Y.-N. Gong, X. Guan, H.-L. Jiang, Covalent organic frameworks for photocatalysis: synthesis, structural features, fundamentals and performance, Coord. Chem. Rev. 475 (2023) 214889.
- [16] B. Song, W.-T. Song, Y.-H. Liang, Y. Liu, B.-W. Li, H. Li, L. Zhang, Y.-H. Ma, R.-Q. Ye, B.-Z. Tang, D. Zhao, Y. Zhou, B. Liu, Direct synthesis of topology-controlled BODIPY and CO₂-based zirconium metal-organic frameworks for efficient photocatalytic CO₂ reduction, Angew. Chem. Int. Ed. 64 (2025) e202421248.
- [17] J. Li, H. Huang, W. Xue, K. Sun, X. Song, C. Wu, L. Nie, Y. Li, C. Liu, Y. Pan, H.-L. Jiang, D. Mei, C. Zhong, Self-adaptive dual-metal-site pairs in metal-organic frameworks for selective CO₂ photoreduction to CH₄, Nat. Catal. 4 (2021) 719–729
- [18] X.-Y. Lu, P. Wang, Z.-F. Qiu, W.-Y. Sun, Cr-MOF composited with facet-engineered bimetallic alloys for inducing photocatalytic conversion of CO₂ to C₂H₄, Chem. Commun. 61 (2025) 2087.
- [19] F. Guo, Y.-P. Wei, S.-Q. Wang, X.-Y. Zhang, F.-M. Wang, W.-Y. Sun, Pt nanoparticles embedded in flowerlike NH₂-UiO 68 for enhanced photocatalytic carbon dioxide reduction, J. Mater. Chem. A 7 (2019) 26490.
- [20] F. Li, D. Wang, Q. Xing, G. Zhou, S.-S. Liu, Y. Li, L.-L. Zheng, P. Ye, J.-P. Zou, Design and syntheses of MOF/COF hybrid materials via postsynthetic covalent modification: an efficient strategy to boost the visible-light-driven photocatalytic performance, Appl. Catal. B 243 (2019) 621–628.
- [21] F.-M. Zhang, J.-L. Sheng, Z.-D. Yang, X.-J. Sun, H.-L. Tang, M. Lu, H. Dong, F.-C. Shen, J. Liu, Y.-Q. Lan, Rational design of MOF/COF hybrid materials for photocatalytic H₂ evolution in the presence of sacrificial electron donors, Angew. Chem. Int. Ed. 57 (2018) 12106–12110.
- [22] X.-Y. Chu, S.-K. Liu, B.-B. Luan, Y. Zhang, Y.-M. Xi, L.-H. Shao, F.-M. Zhang, Y.-Q. Lan, Crystal-facet-controlled internal electric field in MOF/COF heterojunction towards efficient photocatalytic overall water splitting, Angew. Chem. Int. Ed. (2025) e202422940.
- [23] Y. Chen, D. Yang, B. Shi, W. Dai, H. Ren, K. An, Z. Zhou, Z. Zhao, W. Wang, Z. Jiang, In situ construction of hydrazone-linked COF-based core-shell heteroframeworks for enhanced photocatalytic hydrogen evolution, J. Mater. Chem. A 8 (2020) 7724–7732.
- [24] C.-X. Chen, Y.-Y. Xiong, X. Zhong, P.-C. Lan, Z.-W. Wei, H.-J. Pan, P.-Y. Su, Y.-J. Song, Y.-F. Chen, A. Nafady, S.-Q. Sirajuddin, Enhancing photocatalytic hydrogen production via the construction of robust multivariate ti-MOF/COF composites, Angew. Chem. Int. Ed. 61 (2022) e202114071.
- [25] L. Wang, J. Mao, G. Huang, Y. Zhang, J. Huang, H. She, C. Liu, H. Liu, Q. Wang, Configuration of hetero-framework via integrating MOF and triazine-containing COF for charge-transfer promotion in photocatalytic CO₂ reduction, Chem. Eng. J. 446 (2022) 137011.
- [26] Q. Niu, S. Dong, J. Tian, G. Huang, J. Bi, L. Wu, Rational design of novel COF/MOF s-scheme heterojunction photocatalyst for boosting CO₂ reduction at gas-solid interface, ACS Appl. Mater. Interfaces 14 (2022) 24299–24308.
- [27] C.-H. Dai, T. He, L.-X. Zhong, X.-G. Liu, W.-L. Zhen, C. Xue, S.-Z. Li, D.-L. Jiang, B. Liu, 2,4,6-Triphenyl-1,3,5-triazine based covalent organic frameworks for photoelectrochemical H₂ evolution, Adv. Mater. Interfaces 8 (2021) 2002191.

- [28] M.-T. Ming, Y.-C. Wang, W.-X. Tao, W.-J. Shi, D.-C. Zhong, T.-B. Lu, Designing dual-atom cobalt catalysts anchored on amino-functionalized MOFs for efficient CO₂ photoreduction, Green Chem. 25 (2023) 6207–6211.
- [29] P.-M. Stanley, J. Haimerl, C. Thomas, A. Urstoeger, M. Schuster, N.-B. Shustova, A. Casini, B. Rieger, J. Warnan, R.-A. Fischer, Host-guest interactions in a metalorganic framework isoreticular series for molecular photocatalytic CO₂ reduction, Angew. Chem. Int. Ed. 60 (2021) 17854–17860.
- [30] X.-W. Lan, H.-S. Li, Y.-M. Liu, Y.-Z. Zhang, T.-J. Zhang, Y. Chen, Covalent organic framework with donor¹-acceptor-donor² motifs regulating local charge of intercalated single cobalt sites for photocatalytic CO₂ reduction to syngas, Angew. Chem. Int. Ed. 63 (2024) e202407092.
- [31] K. Choe, F.-B. Zheng, H. Wang, Y. Yuan, W.-S. Zhao, G.-X. Xue, X.-Y. Qiu, M. Ri, X.-H. Shi, Y.-L. Wang, Y.-D. Li, Z.-Y. Tang, Fast and selective semihydrogenation of alkynes by palladium nanoparticles sandwiched in metal-organic frameworks, Angew. Chem. Int. Ed. 59 (2020) 3650–3657.
- [32] Y.-L. Yang, Y.-R. Wang, L.-Z. Dong, Q. Li, L. Zhang, J. Zhou, S.-N. Sun, H.-M. Ding, Y. Chen, S.-L. Li, Y.-Q. Lan, A honeycomb-like porous crystalline hetero-electrocatalyst for efficient electrocatalytic CO₂ reduction, Adv. Mater. 34 (2022) 2206706.
- [33] Y. Wang, Z. Zhang, L. Zhang, Z. Luo, J. Shen, H. Lin, J. Long, J.C.S. Wu, X. Fu, X. Wang, C. Li, Visible-light driven overall conversion of CO₂ and H₂O to CH₄ and O₂ on 3D-SiC@2D-MoS₂ heterostructure, J. Am. Chem. Soc. 140 (2018) 14595–14598.
- [34] J. Bian, Z. Zhang, J. Feng, M. Thangamuthu, F. Yang, L. Sun, Z. Li, Y. Qu, D. Tang, Z. Lin, F. Bai, J. Tang, L. Jing, Energy platform for directed charge transfer in the cascade z-scheme heterojunction: CO₂ photoreduction without a cocatalyst, Angew. Chem. Int. Ed. 60 (2021) 20906–20914.
- [35] J.-J. Liu, S.-N. Sun, J. Liu, Y. Kuang, J.-W. Shi, L.-Z. Dong, N. Li, J.-N. Lu, J.-M. Lin, S.-L. Li, Y.-Q. Lan, Achieving high-efficient photoelectrocatalytic degradation of 4chlorophenol via functional reformation of titanium-oxo clusters, J. Am. Chem. Soc. 145 (2023) 6112–6122.
- [36] J. Ding, X. Guan, J. Lv, X. Chen, Y. Zhang, H. Li, D. Zhang, S. Qiu, H.-L. Jiang, Q. Fang, Three-dimensional covalent organic frameworks with ultra-large pores for highly efficient photocatalysis, J. Am. Chem. Soc. 145 (2023) 3248–3254.
- [37] L. Shi, P. Li, W. Zhou, T. Wang, K. Chang, H. Zhang, T. Kako, G. Liu, J. Ye, N-type boron phosphide as a highly stable, metal-free, visible-light-active photocatalyst for hydrogen evolution, Nano Energy 28 (2016) 158.
- [38] D.-C. Zhong, Y.-N. Gong, C. Zhang, T.-B. Lu, Dinuclear metal synergistic catalysis for energy conversion, Chem. Soc. Rev. 52 (2023) 3170.

- [39] J.-H. Zhang, Y.-C. Wang, H.-J. Wang, D.-C. Zhong, T.-B. Lu, Enhancing photocatalytic performance of metal-organic frameworks for CO₂ reduction by a bimetallic strategy, Chin. Chem. Lett. 33 (2022) 2065–2068.
- [40] B. Zhang, L. Sun, Artificial photosynthesis: opportunities and challenges of molecular catalysts, Chem. Soc. Rev. 48 (2019) 2216.
- [41] S. Chen, J.J.M. Vequizo, Z. Pan, T. Hisatomi, M. Nakabayashi, L. Lin, Z. Wang, K. Kato, A. Yamakata, N. Shibata, T. Takata, T. Yamada, K. Domen, Surface modifications of (ZnSe)_{0.5}(CuGa_{2.5}Se_{4.25})_{0.5} to promote photocatalytic z-scheme overall water splitting, J. Am. Chem. Soc. 143 (2021) 10633–10641.
- [42] H.S. Moon, K.-C. Hsiao, M.-C. Wu, Y. Yun, Y.-J. Hsu, K. Yong, Spatial separation of cocatalysts on Z-scheme organic/inorganic heterostructure hollow spheres for enhanced photocatalytic H₂ evolution and in-depth analysis of the charge-transfer mechanism, Adv. Mater. 35 (2023) 2200172.
- [43] S. Yoshino, A. Iwase, Y. Yamaguchi, T.M. Suzuki, T. Morikawa, A. Kudo, photocatalytic CO₂ reduction using water as an electron donor under visible light irradiation by Z-scheme and photoelectrochemical systems over (CuGa)_{0.5}ZnS₂ in the presence of basic additives, J. Am. Chem. Soc. 144 (2022) 2323–2332.
- [44] S. Gligorovski, R. Strekowski, S. Barbati, D. Vione, Environmental implications of hydroxyl radicals (•OH), Chem. Rev. 115 (2015) 13051–13092.
- [45] H.-W. Lv, P.-Y. Li, X.-J. Li, A.-C. C, R.-J. Sa, H. Zhu, R.-H. Wang, Boosting photocatalytic reduction of the diluted CO₂ over covalent organic framework, Chem. Eng. J. 451 (2023) 138745.
- [46] M. Zhou, Z.-Q. Wang, A. Mei, Z.-F. Yang, W. Chen, S.-Y. Ou, S.-Y. Wang, K.-Q. Chen, P. Reiss, K. Qi, J.-Y. Ma, Y.-L. Liu, Photocatalytic CO₂ reduction using La-Ni bimetallic sites within a covalent organic framework, Nat. Commun. 14 (2023) 2473
- [47] Q. Li, J.-Nan Chang, Z.-M. Wang, M. Lu, C. Guo, M. Zhang, T.-Y. Yu, Y.-F. Chen, S.-L. Li, Y.-Q. Lan, Modulated connection modes of redox units in molecular junction covalent organic frameworks for artificial photosynthetic overall reaction, J. Am. Chem. Soc. 145 (2023) 23167–23175.
- [48] S.-Q. Gao, Q. Zhang, X.-F. Su, X.-K. Wu, X.-G. Zhang, Y.-Y. Guo, Z.-Y. Li, J.-S. Wei, H.-Y. Wang, S.-J. Zhang, J.-J. Wang, Ingenious artificial leaf based on covalent organic framework membranes for boosting CO₂ photoreduction, J. Am. Chem. Soc. 145 (2023) 9520–9529.
- [49] L. Liu, H. Meng, Y. Chai, X. Chen, J. Xu, X. Liu, W. Liu, D.M. Guldi, Y. Zhu, Enhancing built-in electric fields for efficient photocatalytic hydrogen evolution by encapsulating C60 fullerene into zirconium-based metal-organic frameworks, Angew. Chem. Int. Ed. 62 (2023) e202217897.
- [50] M. Wang, M. Shen, X. Jin, J. Tian, M. Li, Y. Zhou, L. Zhang, Y. Li, J. Shi, Oxygen vacancy generation and stabilization in GeO₂-x by cu introduction with improved CO₂ photocatalytic reduction activity, ACS Catal. 9 (2019) 4573–4581.